# SEDLOB and PATLOB: Two Numerical Tools for Modeling Climatically-Forced Sediment and Water Volume Transport in Large Ocean Basins

B. J. Haupt, K. Stattegger and D. Seidov

## 1 Introduction

The processes of sediment erosion, transport and deposition in large ocean basins depend strongly on sediment input from various sources and on oceanic circulation patterns. Most sedimentation models developed during the last decade are designed for small basins and specific sediment input simulating alluvial or deltaic basin fill (cf. Bitzer and Pflug 1989; Cao and Lerche 1994; Paola et al. 1992; Slingerland et al. 1994; Syvitzki and Daughney 1992; Tetzlaff and Harbaugh 1989). In order to simulate large basins we need to couple an ocean general circulation model (OGCM) with an sedimentation model.

Oceanic thermohaline circulation is controlled mainly by the morphology of a basin and by climate. Given a specific steady-state oceanic circulation pattern from an OGCM with its temperature, salinity, velocity fields and convection depths, one can add sediment characterized by its physical properties to the circulating water volumes. The proper representation of important topographic features depends on the spatial resolution of the model basin.

With respect to sediments, a numerical model should allow simulation of:

1. sediment distribution patterns on the sea floor, especially accumulation and erosion of sediments integrated over time intervals long enough to represent the stratigraphic architecture; and
2. transport paths of water volumes and defined sediment particles from prescribed sources.

Two numerical models, SEDLOB (SEDimentation in Large Ocean Basins) and PATLOB (PArticle Tracing in Large Ocean Basins) were developed for this purpose. Especially PATLOB is a useful tool to address both sedimentation and deep ocean ventilation problems. In this chapter, the structure and most important algorithms of these models are described and applied to the modern North Atlantic. Earlier versions of the models can be found in Haupt (1995) and Haupt et al. (1994, 1995).

J. Harff et al. (eds.), *Computerized Modeling of Sedimentary Systems*

## 2
## The Sediment Transport Model SEDLOB

SEDLOB mainly consists of two coupled submodels which are linked with each other (Fig. 1). The first submodel includes sediment transport in a 3–D water column (Bitzer and Pflug 1990; McCave and Gross 1991; Zanke 1977b), and the second two-dimensional (2-D) submodel simulates the near bottom processes in a 1-cm-thick layer (Puls 1981; Sündermann and Klöcker 1983; Zanke 1978). This 2-D boundary layer is always parallel to the bottom and continuously follows the dynamic changes of the topography. Although the model is used for the deep ocean, the 1-cm thickness is chosen for the bottom layer on the basis of experimental studies of flows in channels. These studies provide detailed information concerning the interdependence between temperature, salinity, viscosity, and velocity. Additionally, the bed and suspension transport are well documented in a set of equations for this 1-cm-thick layer.

### 2.1
### Three-Dimensional Submodel of SEDLOB

The upper 3-D submodel of SEDLOB (Fig. 2) simulates the lateral inflow and outflow of particles from coastal sources as well as the inputs of eolian dust (worldwide approximately 60–360 million tons/year), and melting icebergs (worldwide approximately 100 Mt/year including glaciers) (Allen 1985; Goldschmidt et al. 1992; Möller 1986; Pickard and Emery 1988). Moreover, several biological processes such as dying plankton and fecal pellet production can act as sediment sources.

### 2.2
### Two-Dimensional Submodel of SEDLOB

The 2-D submodel of SEDLOB simulates the exchange of sediment between the water column and the ocean bottom. Within this layer, which follows the bottom

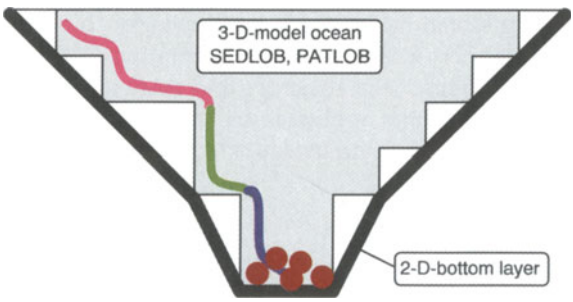


**Fig. 1** Coupling of the two submodels

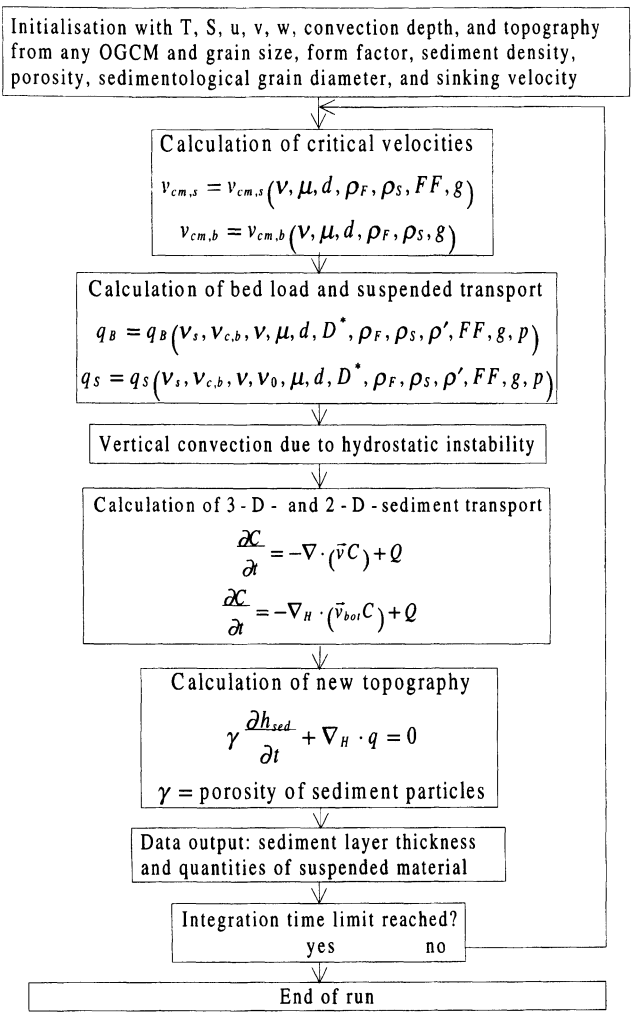


**Fig. 2** Flow chart of SEDLOB

topography, erosion, transport (sliding, rolling, and skipping), and deposition of sediment is calculated based on the critical shear velocities of the bed load and the suspension load, the bottom slope, and bottom roughness (bottom friction) (Anderson and Humphrey 1989; Bogárdi 1974; Garde and Ranga Raju 1977; Hsü 1989; Puls 1981; Sündermann and Klöcker 1983; Zanke 1976; 1977a; 1978; 1982). The change in the bottom topography is calculated from the changing sediment content in the 1-cm-thick bottom layer (Krohn 1975; Sündermann and Klöcker 1983).

## 2.3 Modeled processes depending on scales

Since our knowledge about many geological and biological processes is very limited, we assume a medium grain size homogenous mixture of sediment (Bitzer and Pflug 1989; Sündermann and Klöcker 1983) and that suspended particles in the water column are transported by currents (Bitzer and Pflug 1989). In order to calculate the vertical transport, one should take into account not only the vertical velocity $w$, but also the settling velocity $w_s$ of suspended material. In addition to the vertical transport by upwelling/sinking water, the settling velocity relative to the water motion is superimposed on the water motion to obtain the true particle transport. The settling velocity depends on grain size, density and kinematic viscosity from the surrounding water as well as particle density, form factor and sedimentological grain diameter, and gravitational acceleration (Gibbs et al. 1971; Gibbs 1985; McCave and Gross 1991; Zanke 1977b). It must be emphasized that the vertical velocities are spatially variable, and are not preset fixed values, as in many other models. This is significant, considering that transport and deposition mainly depend on the settling velocity, $w_s$, which normally exceeds the vertical velocity of the surrounding water (Fig. 3; McCave 1984). The movement of sediment is based on mechanical processes (Dietrich et al. 1975; Miller et al. 1977; Zanke 1982).

Tectonic processes are not considered here because our sedimentation reconstructions cover only geologically short time periods lasting from several hundreds to several thousands of years. During such time intervals, the overall ocean geometry may be considered stationary for the North Atlantic (Wold 1992). Tectonic subsidence or uplift is much slower than the expected sedimentation rate within a range from a few millimeters to several meters over a 1000-year timespan (Shaw and Hay 1989). As a consequence, tectonic movements and their effects on topography are negligible (Stephenson 1989).

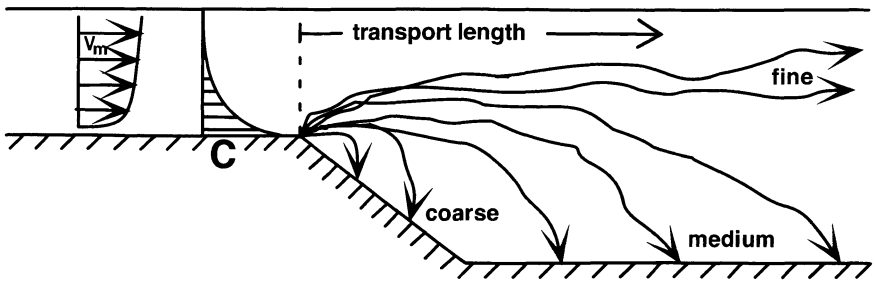


**Fig. 3** Sketch of different transport length due to different grain size, and different settling velocity $w_s$. (After Middleton and Southland 1984)

## 2.4
## Model Equations of SEDLOB

In the following section, the equations of the 3-D and 2-D submodels are listed separately. The symbols and units used are listed in the Appendix. For the sake of clarity, all equations are shown in Cartesian coordinates.

## 2.5
## The Three-Dimensional Submodel of SEDLOB

The 3-D submodel of SEDLOB consists of a transport equation with a source term $Q$ (Bryan 1969; Dietrich et al. 1975; Eppel 1977/78; Fahrbach et al. 1989; Gerdes 1988; Struve 1978; Tetzlaff and Harbaugh 1989)

$$\frac{\partial C}{\partial t} = -\nabla \cdot \left(\vec{v} C\right) + Q \tag{1}$$

and a continuity equation (conservation of mass) for an incompressible medium (and a continuity equation (conservation of mass) for an incompressible medium ( $d\rho_F / dt = 0$ ) (Apel 1987; Bryan 1969; Fahrbach et al. 1989; Kurz 1977; Krauß 1973; LeBlond and Mysak 1978; Pond and Pickard 1986; Tetzlaff and Harbaugh 1989):

$$\nabla \cdot \vec{v} = \frac{\partial u}{\partial x} + \frac{\partial v}{\partial y} + \frac{\partial w}{\partial z}. \tag{2}$$

The hydrostatic equation gives the local pressure $p$ (Bryan 1969; Cox 1984; Haupt 1990):

$$p(z) = p_{surf} + g \int_{z}^{0} \rho_F \, dz. \tag{3}$$

The nonlinear equation of state is given by the UNESCO formula (UNESCO 1981; see also Millero and Poisson 1981)

$$\rho_F = \rho_F\left(T, S, p\right). \tag{4}$$

The settling velocity $w_s$ of a single particle is calculated using the approximation given in Zanke (1977b)

$$w_s = w_s\left(\nu, \mu, d, \rho_F, \varphi_S, FF, g\right)$$

$$= \frac{12\nu}{d\left(2.7 - 2.3FF\right)} \left( \sqrt{1 + \left( 0.21 \left( \frac{\left(\frac{\rho_S - \rho_F}{\rho_F}\right) g}{\nu^2} \right)^{\frac{1}{3}} \right)^3 \left(2.7 - 2.3FF\right)} - 1 \right). \tag{5}$$

The equation for dynamic viscosity $\mu$

$$\mu = \mu(T,S,p) \tag{6}$$

is approximated by a polynom (Matthäus 1972). The total vertical velocity of $w_g$ is the sum of the water velocity and the particle settling velocity:

$$w_g = w + w_s. \tag{7}$$

At the surface, the "rigid-lid" approximation is used:

$$w_{surf} = 0 \quad \text{for} \quad z = 0. \tag{8}$$

The "rigid-lid" approximation eliminates external gravity waves and allows for a longer time step ($\Delta t$) (Cox 1984; Haupt 1990; LeBlond and Mysak 1978). At lateral boundaries "no-flux" and "no-slip" boundary conditions are used:

$$u, v, C_n = 0. \tag{9}$$

No bottom friction is used, but rather a "free-slip" boundary condition is employed at the bottom:

$$\frac{\partial u}{\partial z}, \frac{\partial v}{\partial z} = 0. \tag{10}$$

The fluxes through the bottom and lateral boundaries are set to zero:

$$\frac{\partial T}{\partial n}, \frac{\partial S}{\partial n}, \frac{\partial C}{\partial n} = 0. \tag{11}$$

The vertical velocity $w$ at the bottom is calculated using the continuity equation

$$w = -\left( u\frac{\partial H}{\partial x} + v\frac{\partial H}{\partial y} \right). \tag{12}$$

## 2.6 The Two-Dimensional Submodel of SEDLOB

In many aspects, the 2-D submodel of SEDLOB is similar to the 3-D submodel. The sediment transport at the bottom has the form

$$\frac{\partial C}{\partial t} = -\nabla_H \cdot \left( \vec{v}_{bot} C \right) + Q. \tag{13}$$

The submodel uses the same hydrostatic equation for the local pressure $p$ [cf. Eq. (3)], the same set of nonlinear equations for density [cf. Eq. (4)] and viscos-

ity [cf. Eq. (6)]. Similarly, the total vertical velocity, $w_g$, is the sum of the vertical velocity $w$ [cf. Eq. (2)] and the settling velocity $w_s$ of a single particle [cf. Eq. (5)]. Even though the 1-cm bottom boundary layer is quasi-2-D, this vertical velocity is needed for coupling both submodels.

The critical velocities for sediment transport are approximated by polynominal equations given in Zanke (1977a; Figs. 4, 5). One has to take into account

1. the critical velocities for starting bed load transport

$$\begin{aligned} v_{cm,b} &= v_{cm,b}\left(\nu,\mu,d,\rho_F,\rho_S,g\right) \\ &= 2.8\left(\left(\frac{\rho_S-\rho_F}{\rho_F}\right)g\,d\right)^{0.5} + 14.7\frac{\nu}{d}c \quad \text{where} \quad c=1; \end{aligned} \tag{14}$$

2. the critical velocities for initiating of suspension load transport

$$\begin{aligned} v_{cm,s} &= v_{cm,s}\left(\nu,\mu,d,\rho_F,\rho_S,FF,g\right) \\ &= 8.4\frac{12\nu}{d\left(2.7-2.3FF\right)}\left(\sqrt{1+\left(0.21\left(\frac{\left(\frac{\rho_S-\rho_F}{\rho_F}\right)g}{\nu^2}\right)^{\frac{1}{3}}\right)^3\left(2.7-2.3FF\right)}-1\right); \end{aligned} \tag{15}$$

3. the critical velocity for deposition

$$\begin{aligned} v_{cm,d} &= v_{cm,d}\left(\nu,\mu,d,\rho_F,\rho_S,FF,g\right) \\ &= 3.93\frac{12\nu}{d\left(2.7-2.3FF\right)}\left(\sqrt{1+\left(0.21\left(\frac{\left(\frac{\rho_S-\rho_F}{\rho_F}\right)g}{\nu^2}\right)^{\frac{1}{3}}\right)^3\left(2.7-2.3FF\right)}-1\right). \end{aligned} \tag{16}$$

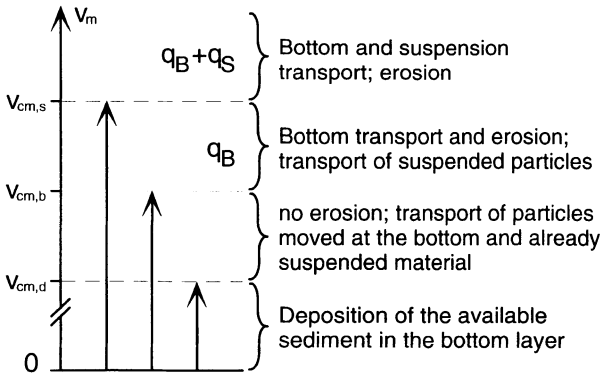


**Fig. 4** Critical velocities for initiating bed load and suspension load transport (cf. Fig. 5)

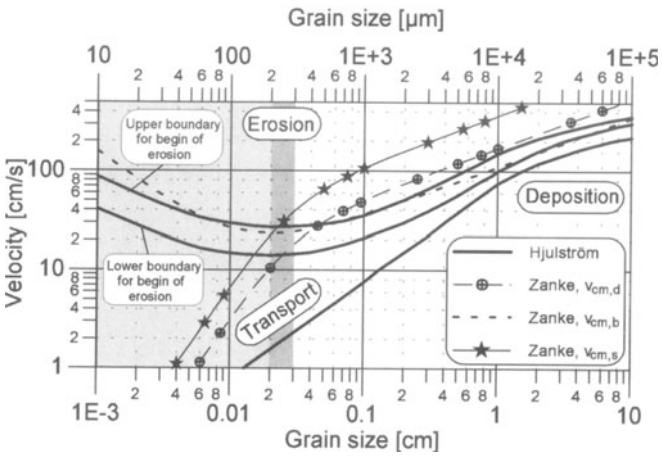


**Fig. 5** Critical velocities for beginning bed load transport and suspension load transport The well-known Hjulström (1935) curve is given as reference

The bed load transport and the suspended load transport are calculated using their dependence on the reduced bottom velocity $\vec{v}_{bot}$ in the 1-cm-thick bottom layer, also called *Prandtl*'s boundary layer (Sündermann and Klöcker 1983; Zanke 1978). The formula for calculating the bed load transport is

$$q_B = q_B\left(v_s, v_{c,b}, \nu, \mu, d, D^*, \rho_F, \rho_S, \rho', FF, g, p\right)$$
$$= \frac{1}{p} 10^{-7} \left( \frac{v_s^2 - v_{c,b}^2}{w_s^2} D^{*2} \right)^2 \nu \quad \text{where} \quad D^* = \left( \frac{\rho' g}{\nu^2} \right)^{\frac{1}{3}} d \quad \text{and} \quad p \approx 0.7, \tag{17}$$

and for calculating the suspension transport is

$$q_S = q_S\left(v_s, v_{c,b}, v_{c,s}, \nu, \nu_0, \mu, d, D^*, \rho_F, \rho_S, \rho', FF, g, p\right)$$
$$= 10^{-8} \frac{H}{h_1} \frac{\left(v_s^2 - v_{c,b}^2\right)\left(v_s^2 - v_{c,s}^2\right)}{w_s^4} D^{*4} \frac{1}{p} \left( \frac{\nu}{\nu_0 - \nu} \right)^{\frac{1}{4}}. \tag{18}$$

The total sediment transport is computed by summing Eqs. (17) and (18):

$$q = q_B + q_S. \tag{19}$$

The relationship of critical velocities and sediment transport is summarized in Fig. 4.

A diagram of critical velocities versus grain size is displayed in Fig. 5.

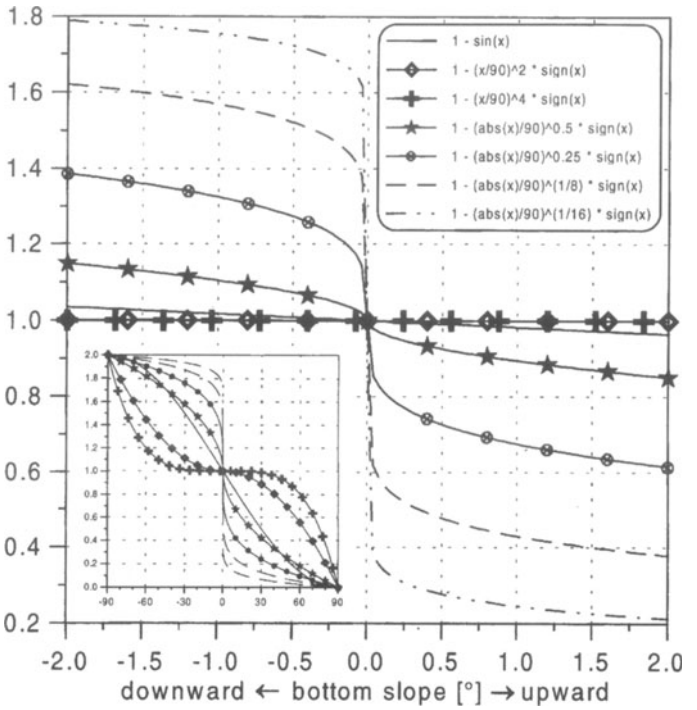


**Fig. 6** Modification of sediment transport and critical velocities. The main figure shows the used functions in a range from –2° to 2°, while the lower left figure shows the range from –90° to 90°, and the upper right box gives the functions embedded in the model

The set of equations dealing with the critical velocities and the sediment transport are modified by the bottom slope. A downward flow leads to an increase in the transport capacities and a decrease in the critical velocities described above and vice versa. This modification is achieved by multiplying the transport velocities by an empirical function dependent on the bottom slope (Haupt 1995; Fig. 6).

The change in the bottom topography due to erosion and deposition is computed using the sediment continuity equation (Sündermann and Klöcker 1983; Tetzlaff and Harbaugh 1989):

$$\gamma \frac{\partial h_{sed}}{\partial t} + \nabla_H \cdot q = 0. \tag{20}$$

Sediment can be eroded or deposited according to Gross and Dade (1991) and Tetzlaff (1989)

$$\frac{\partial h_{sed}}{\partial t} < 0 \quad \text{erosion}$$
$$\frac{\partial h_{sed}}{\partial t} > 0 \quad \text{deposition.} \tag{21}$$

This technique makes the simulation of the process of redistribution of the already deposited sediment possible (Frohlich and Matthews 1991). Sediment is neither eroded nor deposited when an equilibrium between the sediment transport and the sediment load exists. The equilibrium is checked at every time step in our model.

## 2.7 Coupling of SEDLOB's submodels

The coupling of both submodels facilitates the sediment exchange between suspension load in the 3-D water column and the bottom layer (Fig. 7). The 2-D bottom layer is initialized at every grid point (i, j) with the data of the 3-D submodel of SEDLOB. This is achieved by projecting the deepest "water grid point" of the 3-D submodel onto the bottom. Since the projected velocity may belong to different layers, the resulting 2-D velocity field is very inhomogeneous in areas where steep gradients in the bottom topography exist. To obtain a smoother flow, the velocity field is smoothed, using a moving average technique. In a large set of numerical experiments, it was found that smoothing with five to ten passes is sufficient to obtain an adequate velocity field in the bottom layer. The smoothed bottom velocity enables the model to run for more than 500 years

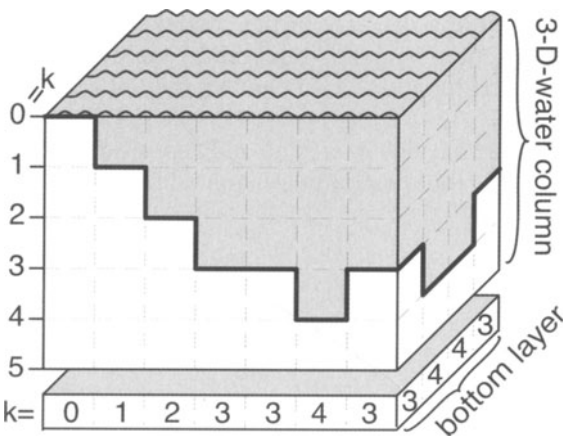


**Fig. 7** Projection and coupling of both submodels

without producing ripples and spikes of sediment transport capacity in the adjacent grid points. Additional smoothing of other fields (bottom topography, sediment concentration near bottom, etc.) is therefore not required.

## 2.8 Numerical design

SEDLOB uses a staggered *Arakawa*-B-grid with a half grid distance's shift between *T–S* points and *u–v* points (Cox 1984; Mesinger and Arakawa 1976), and a Cartesian coordinate system with the vertical axis directed downward. The time integration is carried out using an "upstream differencing" scheme (Mesinger and Arakawa 1976; Struve 1978). This scheme is known to be rather effective (Dube et al. 1986), and may become essential for long-term integrations. It should be noted that this scheme, which is also called the donor cell, upward, or upwind scheme, is positive definite: positive values, like concentration, always remain positive during integration ["possitivity"; ( $C_i^0 \geq 0$ for all $i$) $\rightarrow$ ( $C_i^N \geq 0$ for all $i$ and $N$)] (Eppel 1977/78; Smolarkiewicz 1983). This is an important feature for mass transports, e.g., the transport of marine and eolian sediments, vapor, or gas in the atmosphere all are positive definite. Using second-order or higher-order integration accuracy schemes can introduce some difficulties because of a negative solution of the equation results (Smolarkiewicz 1983). Furthermore, a given disturbance is transported in the direction of physical advection and not, as in other discretization schemes, in the opposite direction (Mesinger and Arakawa 1976; Struve 1978). Furthermore, the "upstream differencing" scheme is mass conservative. All these requirements are only satisfied if the *Courant-Friedrichs-Levy* criterion is not violated (Eppel 1977/78; Mesinger and Arakawa 1976; Smolarkiewicz 1983; Struve 1978):

$$c_x \geq u\frac{\Delta t}{\Delta x}, c_y \geq v\frac{\Delta t}{\Delta y}, c_z \geq w_g\frac{\Delta t}{\Delta z}, \tag{22}$$

where $c_x$, $c_y$,$c_z$ are Courant numbers ($c_{x,y,z} \leq 1$).Thus, the maximum time step in the model is:

$$\Delta t \leq \min\left(\frac{dx_{i,j}}{|u_{i,j,k}|}, \frac{dy_{i,j}}{|v_{i,j,k}|}, \frac{dz_k}{|w_{g\,i,j,k}|}\right). \tag{23}$$

Here $dx_{i,j}$, $dy_{i,j}$, $dz_k$ denote the grid steps. The three velocity components are by $u_{i,j,k}$, $v_{i,j,k}$ and $w_{g_{i,j,k}}$.

Because a normal "upwind"-scheme has a strong implicit diffusion, we modify it in the 2-D submodel. There are different schemes to overcome the deficiencies of the simple upwind formulation. For example, the self-adjusting hybrid scheme (SASH), or the flux correction technique (FCT) offer better functionality while retaining the advantages of the upward scheme. However, the usefulness

of these schemes is rather limited because of excessive computer time required. In addition, a positive definite solution is not guaranteed. Yet any emerging negative values are small enough to be neglected (Smolarkiewicz 1983; Struve 1978). An appropriate numerical scheme is essential for obtaining "sediment fronts", produced by sediment slumps, or local sediment clouds, etc. Smolarkiewicz (1983) introduces an "antidiffusion" with an "antidiffusion velocity" to keep the fronts sharp in spite of the high artificial diffusion inherent to the upwind schemes.

The numerical advection scheme is illustrated below for one-dimensional advection only. In a normal upwind scheme, two terms are in balance: the local changes in time, and the advective term. Smolarkiewicz (1983) adds another term with a small implicit diffusion at a low computational cost:

$$\underbrace{\frac{\partial C}{\partial t}+\frac{\partial}{\partial x}(uC)}_{\text{normal upwind scheme}} = \underbrace{\frac{\partial}{\partial x}\left(K_{impl}\frac{\partial C}{\partial x}\right)}_{\text{implicit diffusion}}, \quad \text{where} \quad K_{impl}=0.5\left(|u|\Delta x-\Delta t\,u^2\right). \tag{24}$$

Thus, for the normal upwind scheme in the 3-D submodel the following discretization on a staggered grid is chosen:

$$C_{n+1,i}=C_{n,i}-\left\{F\left(C_{n,i},C_{n,i+1},u_{n,i+\frac{1}{2}}\right)-F\left(C_{n,i-1},C_{n,i},u_{n,i-\frac{1}{2}}\right)\right\}, \tag{25}$$

where

$$F\left(C_i,C_{i+1},u\right)=\left[\left(u+|u|\right)C_i+\left(\left(u-|u|\right)C_{i+1}\right)\right]\frac{\Delta t}{2\Delta x}. \tag{26}$$

In the 2-D submodel we use the scheme of Smolarkiewicz (1983) with $\tilde{u}$ as antidiffusion velocity. The function $F$ has the same form as in Eq. (26).

$$C_i^*=C_{n,i}-\left\{F\left(C_{n,i},C_{n,i+1},u_{n,i+\frac{1}{2}}\right)-F\left(C_{n,i-1},C_{n,i},u_{n,i-\frac{1}{2}}\right)\right\} \tag{27}$$

$$C_{n+1,i}=C_i^*-\left\{F\left(C_i^*,C_{i+1}^*,\tilde{u}_{n,i+\frac{1}{2}}\right)-F\left(C_{i-1}^*,C_i^*,\tilde{u}_{n,i-\frac{1}{2}}\right)\right\}, \tag{28}$$

where

$$\tilde{u}_{i+\frac{1}{2}}=\frac{\left(\left|u_{i+\frac{1}{2}}\right|\Delta x-\Delta t u_{i+\frac{1}{2}}^2\right)\left(C_{i+1}^*-C_i^*\right)}{\left(C_i^*+C_{i+1}^*+\varepsilon\right)\Delta x}. \tag{29}$$

$\varepsilon$ is a small value (here $10^{-15}$) to ensure $\tilde{u}=0$ when $C_{i+1}^*=C_i^*=0$.

A growth or decay of the initial signal can be obtained by scaling the antidiffusion velocity $\tilde{u}$ by a factor *Sc*:

$$\tilde{u}_{scale} = Sc\,\tilde{u} \tag{30}$$

The best result was achieved using a scaling factor of $1 \leq Sc \leq 1.08$ after Smolarkiewicz (1983). With $Sc = 0$ the above described scheme is identical to the normal upwind scheme without antidiffusion. Three experiments with different scaling factors are discussed below. These experiments were carried out to demonstrate how antidiffusion works and to check the program's overall performance. Starting from a given distribution of sediment in an anticyclone velocity field, the calculations are shown for one full rotation around the center (Fig. 8). The first experiment (I) has been carried out without antidiffusion $Sc = 0$, the second one (II) with a scaling factor $Sc = 1$, and the third one (III) with a factor $Sc = 1.08$ (Figs. 9, 10). With a scaling factor $Sc = 1$ we obtain results similar to those obtained by Smolarkiewicz (1983), i.e., best fit. The horizontal extent and intensity of the initial perturbation was preserved with good accuracy.

Without antidiffusion (experiment I) the experiment suffers from strong diffusion, which results in the signal being flattened and expanded horizontally. When the antidiffusion was overestimated, the initial perturbation was deformed and new maxima appeared (experiment III). It should be stressed that mass was conserved in all experiments.

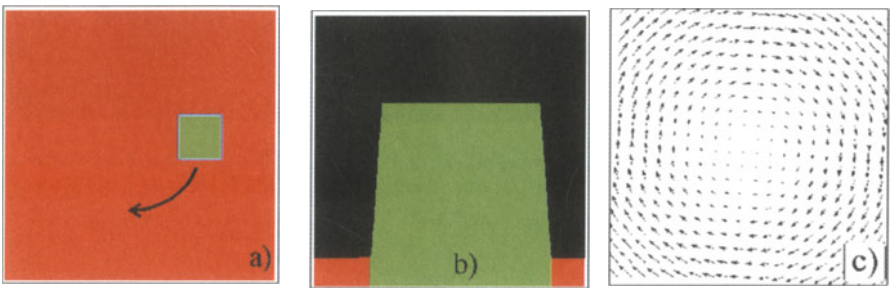


**Fig. 8a–c** Sediment distribution of the three experiments I, II, and III as a map view (**a**) and as a sectional view (**b**). The velocity field is circular (**c**)

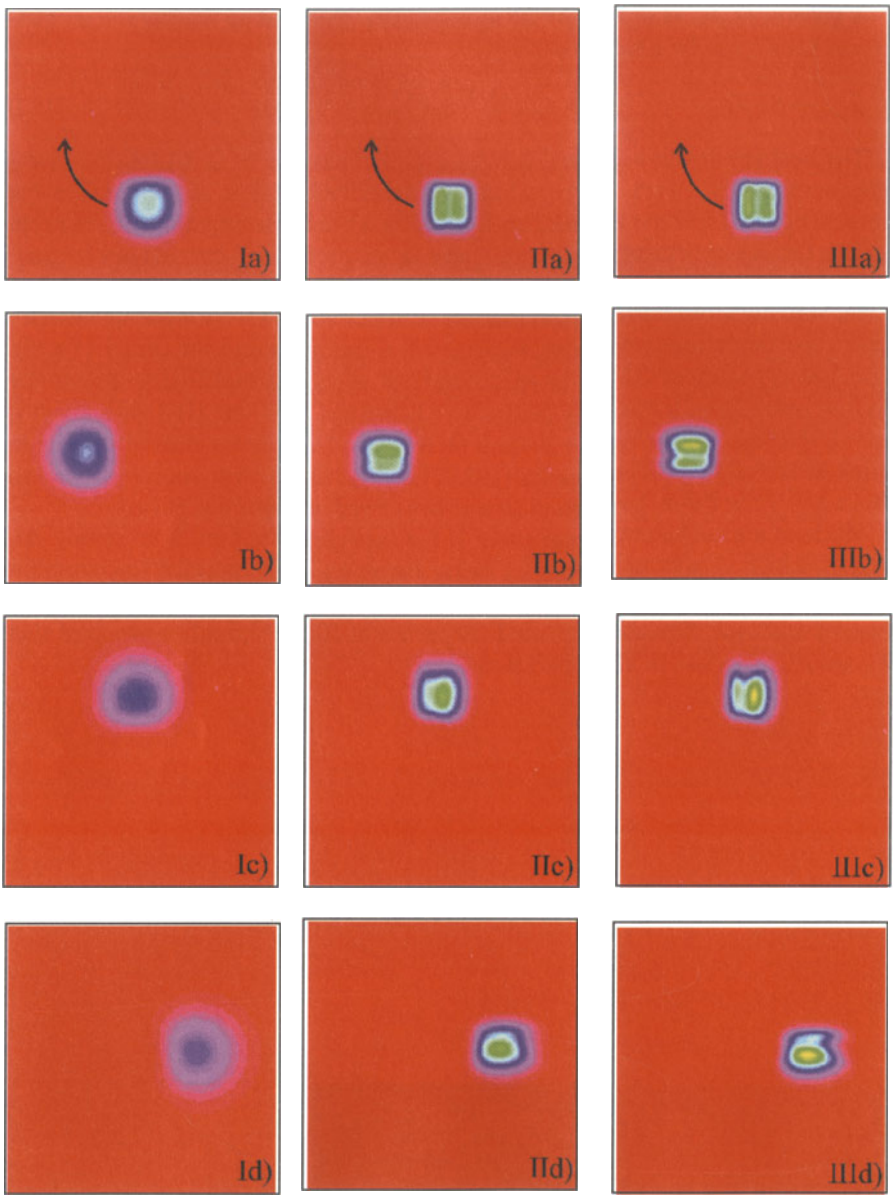


**Fig. 9** Sediment distribution of the three experiments I, II, and III as a map view. Experiment I is calculated without antidiffusion ($Sc = 0$), the experiments II ($Sc = 1$), and III ($Sc = 1.08$) are calculated with antidiffusion (Smolarkiewicz 1983)

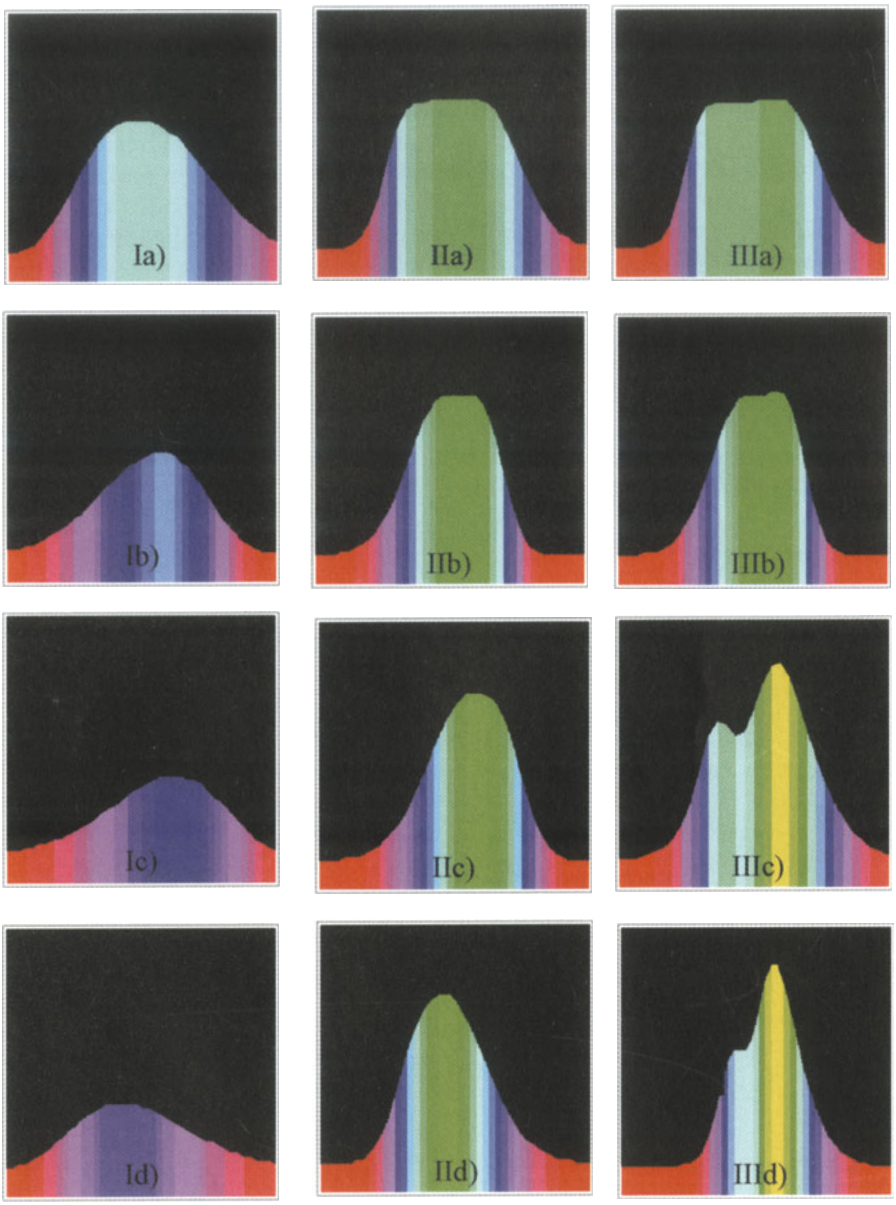


**Fig. 10** Sediment distribution of the three experiments I, II, and III as a sectional view. Experiment I is calculated without antidiffusion ($Sc = 0$), the experiments II ($Sc = 1$), and III ($Sc = 1.08$) are calculated with antidiffusion (Smolarkiewicz 1983)

## 3
## The particle-tracing model PATLOB

The semi-Lagrangian (hybrid Eulerian-Lagrangian approach) model PATLOB (Fig. 11) traces material parcels, e.g., water parcels, sediments, pollutants, natural or artificial organic material, etc. from their source area/origin until they are dissolved or deposited. This model is a useful tool to address both sedimentation and deep ocean ventilation problems. PATLOB was developed in order to use semi-Lagrangian calculations in combination with SEDLOB, which uses the output of the OGCM. Thus, the assumptions made for PATLOB are similar to those made for SEDLOB. Like SEDLOB, PATLOB mainly consists of two coupled submodels which are linked together. Hence, data flow between two submodels and the projection of data onto the 2-D 1-cm-thick bottom layer works identically in SEDLOB and PATLOB. Additionally, PATLOB takes the change in the bottom topography into account, which is calculated with SEDLOB. This is also relevant to particles which have a settling velocity.

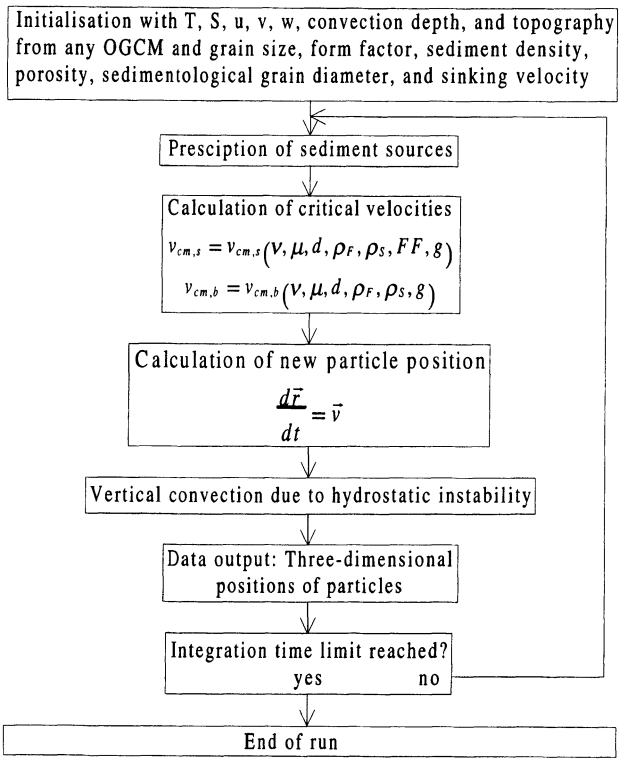


**Fig. 11** Flow chart of PATLOB

### 3.1
### Formulation of PATLOB

PATLOB uses the same approximation for the settling velocity, $w_s$, the critical shear velocities of bed load ($v_{cm,b}$) and suspension load ($v_{cm,s}$), and the critical velocity $v_{cm,d}$ for a final deposition of the parcels found in SEDLOB. Furthermore, the critical velocities are updated by the bottom slope.

The new location of every particle is calculated from the old position (Goldstein 1985; Kurz 1977):

$$\frac{d\vec{r}}{dt} = \vec{v}. \tag{31}$$

For the 3-D submodel the equation above is written in Cartesian coordinates as

$$\begin{aligned} r_{x,n+1} &= r_{x,n} + u_r \, \Delta t \\ r_{y,n+1} &= r_{y,n} + v_r \, \Delta t \\ r_{z,n+1} &= r_{z,n} + w_{g_r} \, \Delta t, \end{aligned} \tag{32}$$

and for the 2-D submodel as

$$\begin{aligned} r_{bot,x,n+1} &= r_{bot,x,n} + u_{bot,r} \, \Delta t \\ r_{bot,y,n+1} &= r_{bot,y,n} + v_{bot,r} \, \Delta t, \end{aligned} \tag{33}$$

where $r$ is used for the location interpolated inside of the numerical grid and $n$ for the time step. This means that the velocity components provided by the OGCM are interpolated to the current position of the Lagrangian particle from nearby points on the Eulerian numerical grid.

## 4
## The vertical convection in SEDLOB and PATLOB

SEDLOB and PATLOB take into account vertical convection. This is an important feature because convection does not transport water and sediment in the same way as advection does. Tracers are advected by currents, whereas convection due to hydrostatic instability mixes water, sediments, and the tracers vertically in "turbulent" water columns or "chimneys" (Fig. 12). The convection due to hydrostatic instability determines the depth of vertical mixing in the ocean. In the model, the convection depth indicates how many layers participate in mixing, that is to which layer a particle entering such a turbulent water column is propelled within the chimney. We use different techniques to introduce this mixing into the two models. In SEDLOB, the sediment concentrations of vertical grid boxes affected by the convection depth are mixed to obtain a homogenous sediment distribution in every time step. In PATLOB, a parcel entering a chimney at the top is propelled downward to the base of the chimney and vice versa. This is equivalent to the reflection of every particle around the middle depth of a con-

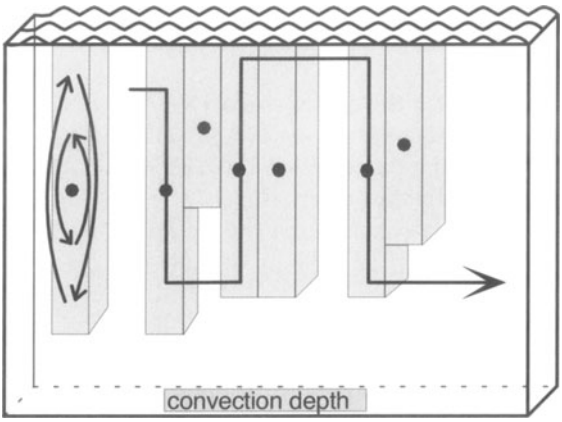


**Fig. 12** Sketch of two particles entering an area with different vertical convection depths (Seidov and Haupt 1997)

vection site. If a particle enters a convection site, it is only mixed once. The vertical position remains unchanged if the particle enters an adjacent convection column having the same convection depth; in a case where the convection is deeper, the particle is brought to its new depth, either upward, or downward (Fig. 12). Additional details of this technique for incorporating convection into SEDLOB and PATLOB are given in Seidov and Haupt (1997).

## 5
## Validation of SEDLOB and PATLOB

The models were originally developed and designed to study sedimentation processes in the North Atlantic and to be integrated with paleoceanographic modeling (Haupt 1995; Haupt et al. 1994, 1995). Therefore, the control experiments presented here concentrate on the modern North Atlantic. We review the results based on model runs with a 0.5°×0.5° horizontal resolution (95 grid points in both horizontal directions). For calculating the sediment transport through gateways and cross-sections, e.g. the Denmark Strait, the Iceland-Faeroe-Scotland-Ridge, or Barents Sea inflow and outflow, it is important to use a high vertical resolution which represents the topography in a realistic manner. Therefore, we use a model topography derived from the *ETOPO5* (1986) data set (Fig. 13) with 17 vertical layers which are 50, 50, 50, 50, 100, 100, 100, 250, 250, 250, 250, 500, 500, 500, 500, 500, and 1000 mthick. The maximum bottom slope in the direction of flow is less than 2.65°. The staircase-type bottom topography must never exceed 5° (Puls 1981), otherwise the turbulent bottom flow will detach from the seabed and the equation for sediment transport [Eq. (20)] will no longer be valid (Fig. 14). We use a spherical coordinate system in which the equator has been rotated up to 60°N along zero meridian in order to minimize the convergence of meridians in high latitudes.

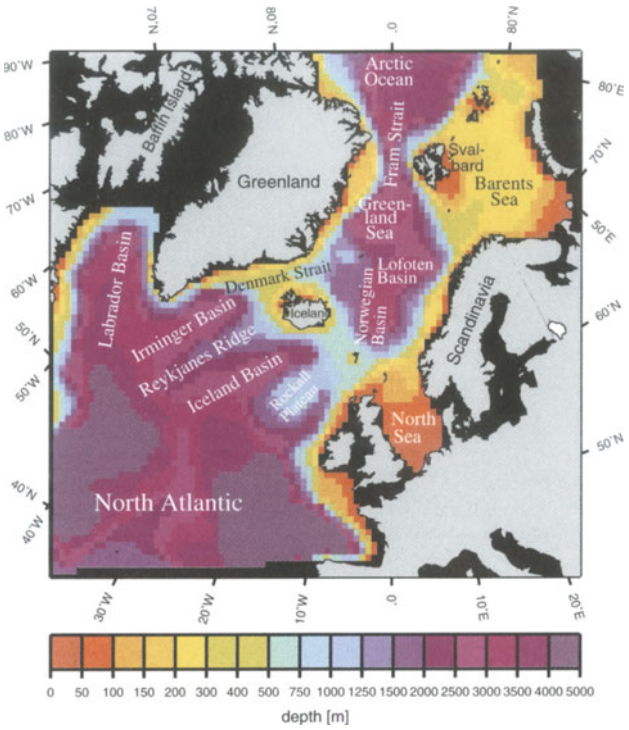


**Fig. 13** Modern model bottom topography of the northern North Atlantic on a 0.5° × 0.5° grid with 17 unevenly spaced vertical layers

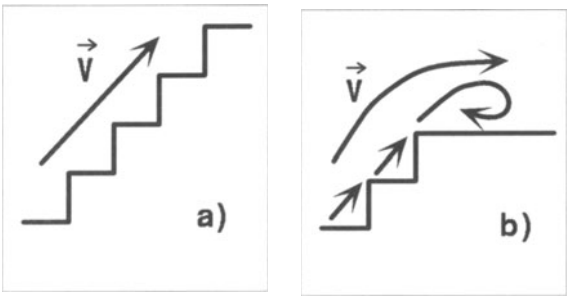


**Fig. 14a, b** Sketch of currents at the staircase bottom topography without a detached sediment transport (**a**). In the case of a detachment, the bottom transport is in the opposite direction (Puls 1981)

Furthermore, a high-resolution bottom topography is required for the better understanding of the influence that the additional sediment sources near Iceland and in the Greenland-Iceland-Norwegian Seas have on the sedimentation patterns in the northern North Atlantic.

## 5.1 Model initialization

As outlined above, in order to run the two models, one needs the output of an OGCM: temperature, salinity, velocity, and convection depths. A detailed de-

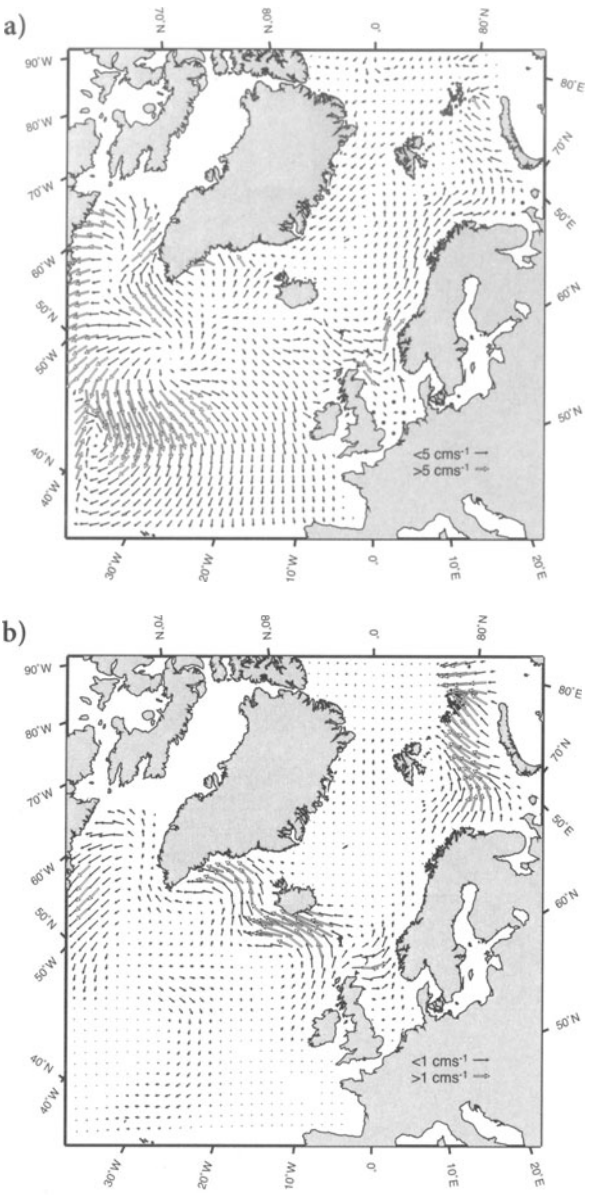


**Fig. 15a, b** Modern velocity: **a** at z=25 m and **b** at the bottom. The bottom velocity in the 1-cm-thick bottom is smoothed with a sliding average with ten passes

scription of the data fields is given in Haupt (1995). Here, we present two examples of the circulation pattern: the first one shows the circulation of the northern North Atlantic at 25 m depth (Fig. 15a), and the second one the bottom circulation resulting from the projection of the 3-D velocity field onto the bottom (Fig. 15b). The bottom velocity is smoothed with a ten-pass sliding average. Although

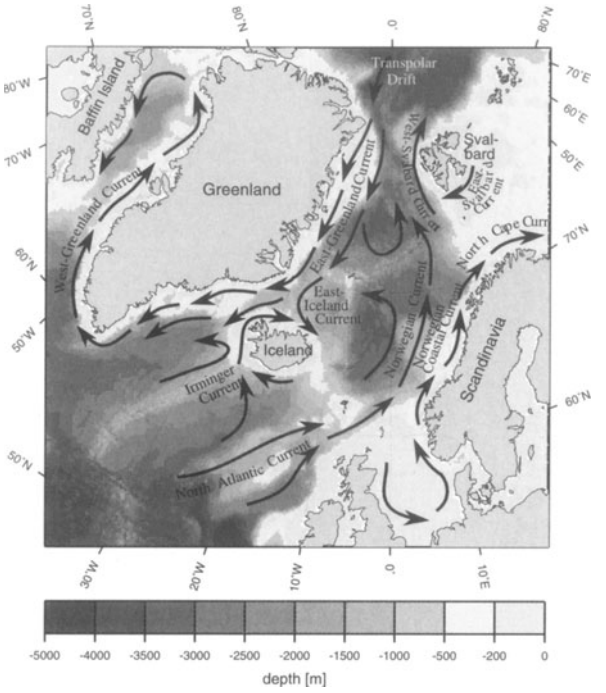


**Fig. 16** The North Atlantic upper ocean circulation pattern

this experiment uses the closed boundary conditions with artificial walls at about 40°N, the model output from the OGCM shows the major currents around Iceland and in the Norwegian-Greenland Seas. These are mainly the West-Greenland Current, the East-Greenland Current, the outflow through the Denmark Strait, the Irminger Current, the North Atlantic Current, the Norwegian Current parallel to the Norwegian Coastal Current which enters the Barents Sea, and the West-Svalbard Current, or the Transpolar Drift (Fig. 16).

The sediment content of the 3-D water column in SEDLOB can be controlled in two different ways: sediment can be manually added to or taken from the water by sources and sinks, or alternatively, the exchange of sediment between the 3-D and the 2-D submodels is calculated automatically. Here, the external source of sediment is prescribed. Sediment sources and quantities inferred from the lateral river input and melting ice sheets are taken from Table 1 (Fig. 17). The lateral river sediment input is restricted to the grid points adjacent to the coastline. To limit the simulations to the case where sediment sources are known only at the lateral boundary, internal sources such as sediment derived from submarine fan deposition or from icebergs and fjords are not considered.

All our experiments were initialized with the same parameters (settling velocity of 0.05 cm $s^{-1}$ = 43.2 m $day^{-1}$ (Shanks and Trent 1980), density of sediment, grain size, and sedimentological grain diameter, form factor of sediment

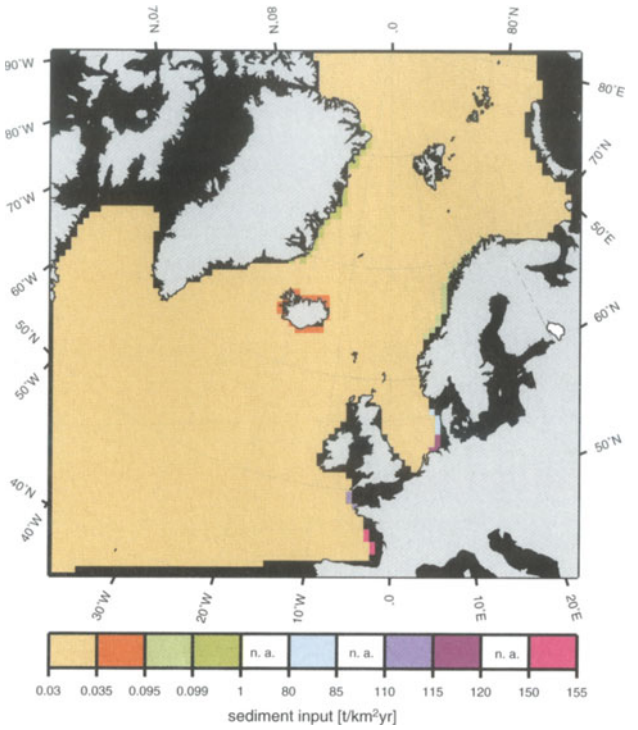


**Fig. 17** Sediment sources prescribed as initial conditions (see Table 1). In the case of conversions the sediment density $\rho_S = 2.6$ cm$^{-3}$ and the porosity $\gamma = 0.75$ were used (Zanke 1982)

**Table 1** Survey of used sediment sources. In case of conversions the sediment density $\rho_S = 2.6$ g/cm$^3$ and the porosity $\gamma = 0.75$ were used (Zanke 1982). The lower sediment input is used in case of a given range (Fig. 17)

| Region | Area [$\times 10^6$ km$^2$] | Sediment input [t/km$^2$ *yr*] | Reference |
|---|---|---|---|
| northern North Atlantic | n. a. | $3.156 \times 10^{-2}$ | Honjo 1990 / Miller et al. 1977 |
| East–Greenland | n. a. | $6.96 \times 10^{-2}$ | Enos 1991 |
| Iceland | n. a. | $6.1 \times 10^{-2}$–$1.085 \times 10^{-1}$ | Enos 1991 |
| Norwegian coast | n. a. | $6.06 \times 10^{-2}$–$6.93 \times 10^{-2}$ | Enos 1991 |
| Elbe | 0.13 | 84 | Milliman / Syvitski 1992 |
| Weser | 0.038 | 33 | Milliman / Syvitski 1992 |
| Seine | 0.065 | 114.2 | Milliman / Syvitski 1992 |
| Loire | 0.155 | 150 | Milliman / Syvitski 1992 |
| southern England | n. a. | < 10 | Einsele 1992 |

particles, and sediment porosity). In both experiments using the sedimentation model SEDLOB, we employed reduced critical velocities to initiate bed load $v_{cm,b}$ and suspension load $v_{cm,s}$. These were set to 0.002 cm $s^{-1}$ and 0.02 cm $s^{-1}$, respectively. In control runs we figured out that a reduction is necessary to obtain realistic transports in the bottom layer in the deeper ocean basins. With these altered initial conditions the model was capable of eroding sediment when the critical velocities were weaker than the velocities predicted by the OGCM. Consequently, it produces more patchy sediment structures. Both simulations were run over 500 years. Unlike the OGCM, it is not possible to run SEDLOB into a steady-state condition. The forward time integration led to continuous changes of the bottom slope and therefore the critical velocities for initiating bed load and suspension load also changed. This is equivalent to the sediment availability which influences the maximum possible sediment concentration and transport in the fluid, depending on the bottom slope inclination.

## 6 Results and Discussion

In the first SEDLOB experiment (E1) only the eolian sediment input from the atmosphere was taken into account (Fig. 18a), whereas the second experiment (E2) added lateral sediment input from rivers and icebergs (Fig. 17). The sedimentation rate is given in cm/1000 years. The locations of the main sediment drifts south of Iceland and south of Greenland are well reproduced (Bohrmann et al. 1990; McCave and Tucholke 1986). However, the sedimentation rate is affected by the chosen distribution of the sediment supply. Both experiments show similar sedimentation patterns. They are mostly formed along the margins of the current axes. Differences can be found especially in regions where strongly selective river sediment input was added to the eolian sediment portion (e.g., in the Bay of Biscay, or in the eastern German Bight). Higher sedimentation rates occur also in the coastal areas, where currents run approximately parallel to the shore line. Here the water takes up a relatively low sediment input and accumulates it while moving along the coast. Whenever coastal currents depart from the coast to the open sea, the speed of the current slows down. Sediment transport capacity decreases and sediments are deposited. This phenomenon is found especially on continental slopes with a downward steepening bottom topography. An example of this is found off Southeast-Greenland where the East-Greenland Current flows through the Denmark Strait into the deep Irminger Basin. This feature can also be found to the south-southeast of Iceland and to the west of Lofoten, where the Norwegian Coastal Current turns to the east into the Norwegian Sea. Sediments are also deposited at higher rates on the Vøring Plateau. The higher sedimentation rates of these shelf areas are in good agreement with the recorded sedimentation rates from sediment cores.

The high sedimentation rate area in the northeasternmost part of the model area has a different origin. In both experiments, E1 (Fig. 18a) and E2 (Fig. 18b), the high sedimentation rates are due to the closed northern boundary and are

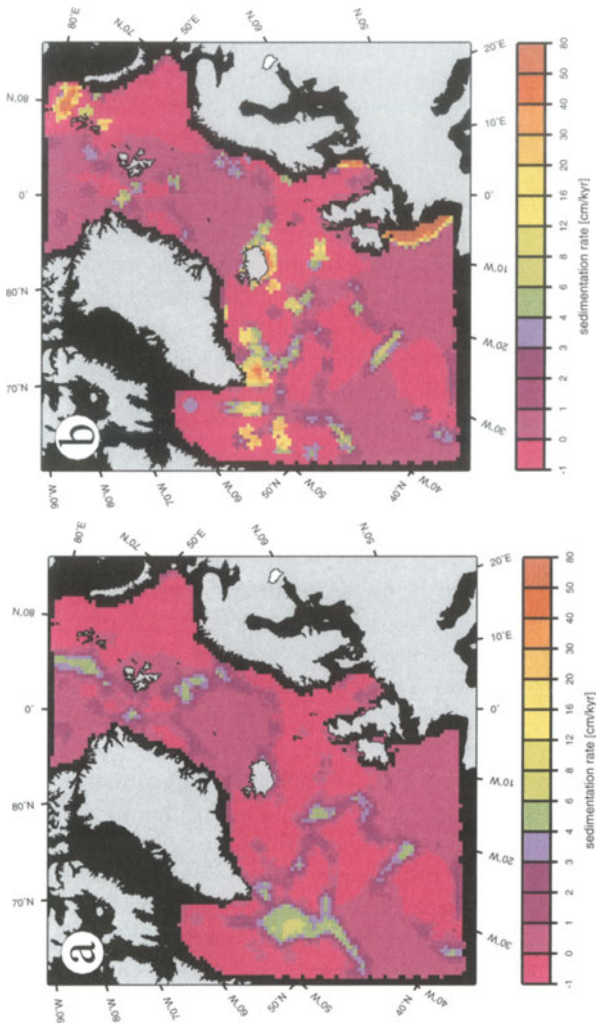


**Fig. 18a, b** Present-day sedimentation rate (cm/1000 years).
**a** Experiment E1: only the eolian sediment input from the atmosphere ($1 \times 10^{-13}$ g cm$^{-2}$ s$^{-1}$ ≈ 0.0864 mg cm$^{-2}$ day$^{-1}$) is considered (Honjo 1990; Miller et al. 1977). The critical velocities for starting of bed load $v_{cm,b}$ and for beginning of suspension load $v_{cm,s}$ are set to 0.002 cm s$^{-1}$ respectively 0.02 cm s$^{-1}$.
**b** Experiment E2: additional sediment sources are applied; see Table 1 and Fig. 17

therefore an artifact. Figures 19 and 20 show the artificial "return flow" east of Franz Josef Land (northeastern Barents Sea). In Figs. 15a, b, 19, and 20, the sediment transport from North Scandinavia by the strong North Cape Current through the Barents Sea can be clearly seen. The southern model boundaries are responsible for artificially low sedimentation rate areas south of 50°N. In the OGCM the inflow of the North Atlantic Current is maintained using a southern sponge layer where the numerical solution is restored to modern climatology in a narrow latitudinal belt near this latitude (Seidov et al. 1996). Because of the lack of information concerning the sediment transport in the water column

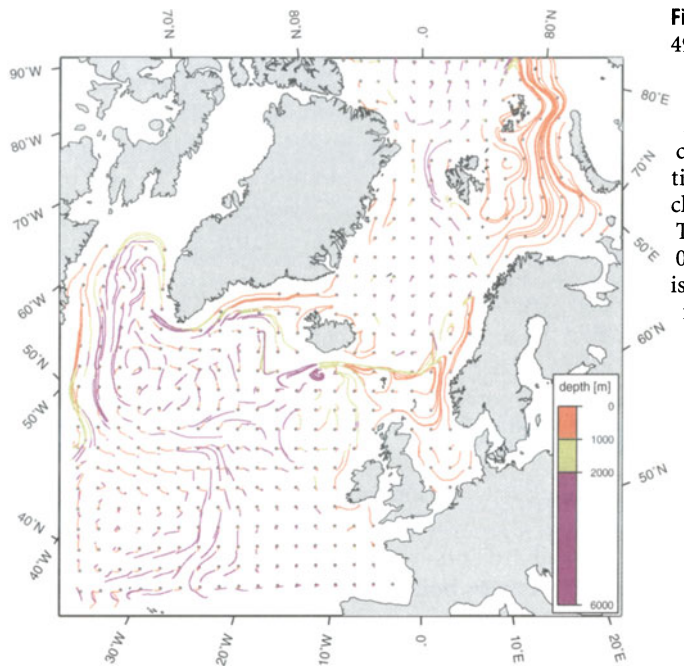


**Fig. 19** Trajectories of 495 Lagrangian particles for the 3-D water motion tracing during 2 years. The small circles show the location where the particles were launched. The settling velocity is 0.05 cm $s^{-1}$. The depth is indicated by colors from the color palette

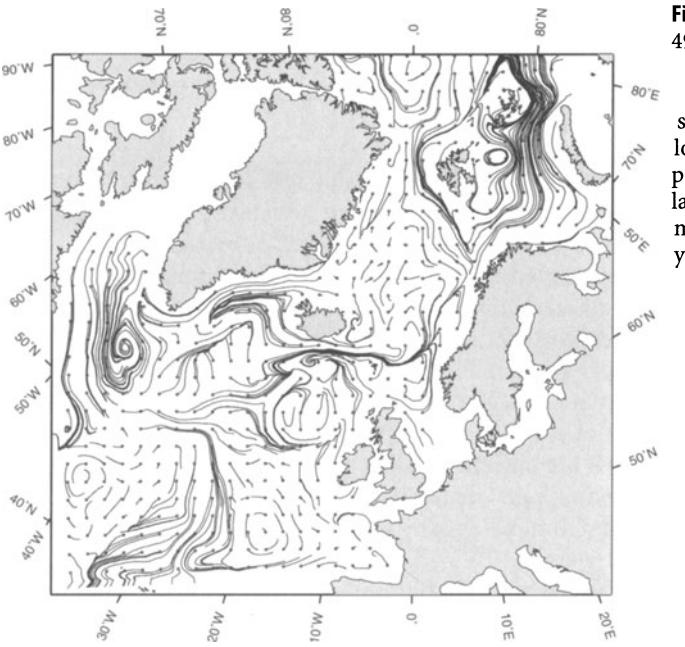

**Fig. 20** Trajectories of 495 Lagrangian particles started in the bottom layer. The small circles show the location where the particles were launched. This experiment was run over 10 years

across these walls, we cannot arrive at reasonable sediment dynamics in this location.

The high sediment input to the English and French shelf areas from southern England and the French rivers Seine and Loire is responsible for the observed high sedimentation rates (Einsele 1992). Contrarily, the runoff from the German rivers Elbe and Weser is not limited to the river mouths. Although most of the sediment is deposited in the eastern German Bight, some is still transported to and deposited in the Norwegian Channel and on the southern Vøring Plateau (63°N, 5°–7°W).

A comparison of the experiments E1 and E2 shows that small local changes in the sediment supply can affect the sediment distribution in remote areas. Theses changes are clearly seen in the transport through gateways and along vertical cross sections. Figure 21a (experiment E1) and Fig. 21b (experiment E2) show the transport in the water column and at the bottom in tons $km^{-2}$ $year^{-1}$. Both experiments indicate that most of the sediment transport occurs in the bottom layer. The transport through the cross section increases with the increase of additional lateral sediment supply everywhere except for two locations. Whether the decrease found between Svalbard and Franz Josef Land is a real feature or an artifact created by the closed northern boundary cannot be answered with this model. In Experiment E2 (Fig. 21b), the bottom transport over the Iceland-Faeroe-Ridge changes from a southward sediment transport (Fig. 21a) to a northward transport. In this region, the currents are generally parallel to the Iceland-Faeroe-Ridge (Figs. 15b, 20). In a set of several supplementary experiments we discovered that a small shift of this cross section to the north or to the south resulted in a change in the transport direction.

## 7 Conclusions

Integrated numerical models of oceanic circulation, sedimentation, and tracing water volumes lead to a better understanding of the complexity of interactions in the climatically forced ocean-sediment system. Two 3-D numerical models, SEDLOB and PATLOB, were developed to reconstruct the sedimentary history of the North Atlantic. Both models consist of a 3-D submodel for the water column and a 2-D bottom layer to model the specific features of near-bottom process motion. The models were tested using different horizontal and vertical resolutions in the North and northeastern Atlantic. High resolution experiments aimed at the simulation of detailed features of sediment flux through gateways and cross sections were discussed. The models are initialized using the output of an OGCM and different sediment sources. We supplied material by vertical eolian input from the atmosphere and from lateral sediment input by rivers and ice. In all experiments, the critical velocities for movement of bed load and suspension load were reduced to arrive at more realistic transports at the bottom in ocean basins. The employed polynominal equations for the sediment transport and the critical velocities were modified by an empirical function to introduce the dependence on bottom slope.

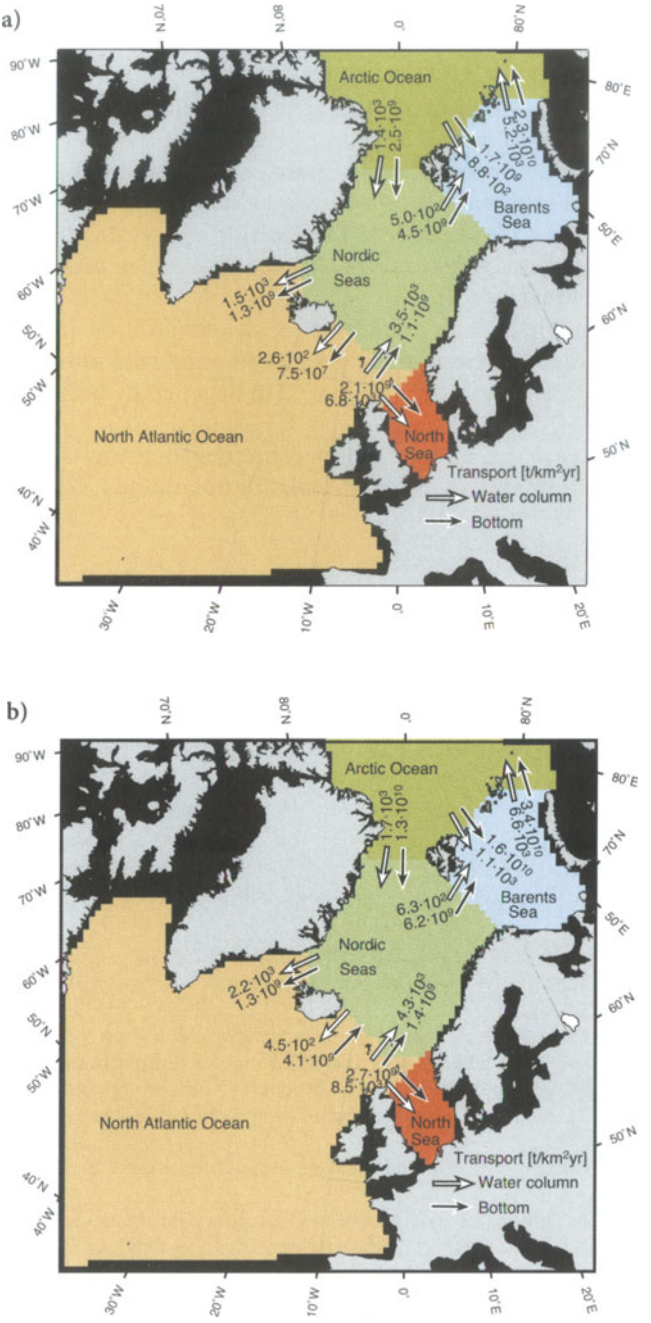


**Fig. 21a, b** Calculated transport rates for the three-dimentional water column and for the bottom layer: experiment E1 (**a**) and experiment E2 (**b**)

The simulated sediment distribution fits well the observed location of the main sediment drifts south of Iceland and Greenland. Additional lateral sediment input did not change the regional distribution of the high sedimentation areas. However, these changes in the input did affect the sedimentation rates and the transport through the cross sections. The increased sediment transport was predicted by the models both in the main body of water, and within the bottom layer. In comparison to the distribution within the water column the transport in the bottom layer showed a weaker response to the addition of lateral sediment sources. The calculation of cross section transport is a valuable tool in mass balancing through oceanic gateways.

In both experiments with SEDLOB we found that coastal downward currents led to reduced bottom current velocities and therefore to a reduced sediment transport capacity. This effect is especially pronounced in the areas of steep bottom gradients.

Finally, we want to emphasize that both models may be coupled to any OGCM which provides the adequate input data fields of temperature, salinity, velocity and convection depth.

### Acknowledgments

This research was supported by the Deutsche Forschungsgemeinschaft (DFG) and SFB313 of Kiel University. We appreciate Avan Antia's und Derek Dreger's help on correcting our English. We thank Johannes Wendebourg for his very useful comments and suggestions which led to improvement of the manuscript.

## References

Allen, J. R. L. (1985) Principles of Physical Sedimentology, George Allen & Unwin, London, 272 pp

Anderson, R. S., and N. F. Humphrey (1989) Interaction of Transport Processes in the Evolution of Arid Landscapes, Quantitative Dynamic Stratigraphy, ed. T. A. Cross, Prentice Hall, Englewood Cliffs, New Jersey, 349–361

Apel, J. R. (1987) Principles of Ocean Physics, Academic Press, London, 38, 634 pp

Bitzer, K., and R. Pflug (1989) DEPOD: A Three-Dimensional Model for Simulating Clastic Sedimentation and Isostatic Compensation in Sedimentary Basins, Quantitative Dynamic Stratigraphy, ed. T. A. Cross, Prentice Hall, Englewood Cliffs, New Jersey, 335–348

Bogárdi, J. L. (1974) Sediment Transport in Alluvial Streams, Akadémiai Kiado, Budapest, 826 pp

Bohrmann, G., R. Henrich, and J. Thiede (1990) Miocene to Quaternary Paleoceanography in the Northern North Atlantic: Variability in Carbonate and Biogenic Opal Accumulation, Geological History of the Polar Oceans: Arctic versus Antarctic, ed. U. Bleil and J. Thiede, Kluwer Academic Publishers, Netherland, 647–675

Bryan, K. (1969) A Numerical Method for the Study of the Circulation of the World Ocean, Journal of Computational Physics, 4, 347–376

Cao, S., and I. Lerche (1994) A Quantitative Model of Dynamical Sediment Deposition and Erosion in Three Dimensions, Computer & Geosiences, 20, 4, 635–663

Cox, M. D. (1984) A Primitive Equation, 3-Dimensional Model of the Ocean, GFDL Ocean Group Technical Report No. 1, Geophysical Fluid Dynamics Laboratory/NOOA, Princeton University

Dietrich, G., K. Kalle, W. Krauß, and G. Siedler (1975) Allgemeine Meereskunde – Eine Einführung in die Ozeanographie, Gebrüder Borntraeger, Berlin, third edition, 593 pp

Dube, S. K., M. E. Luther, and J. J. O'Brien (1986:) Documentation of the FSU Indian Ocean Model, Cooperative Indian Ocean Modelling Project Technical Report, Prepared at Mesoscale Air-Sea Interaction Group, The Florida State University, Tallahassee, FL 32306, 87 pp

Einsele, G. (1992) Sedimentary Basins; Evolution, Facies, and Sediment Budget, Springer-Verlag, Berlin, 628 pp

Enos, P. (1991) Sedimentary Parameters for Computer Modeling, Sedimentary Modeling: Computer Simulation and Methods for Improved Parameter Definition, ed. E. K. Franseen, W. L. Watney, C. G. St. C. Kendall and W. Ross, Kansas Geological Survey, 233, 63–98

Eppel, D. P. (1977/78) Numerische Simulation mesoskaliger Phänomene I., Skriptum zur Vorlesung – gehalten im Institut für Meereskunde an der Universität Kiel, Forschungszentrum Geesthacht GmbH – GKSS, Geesthacht, 105 pp

ETOPO5 (1986) Digital Relief of the Surface of the Earth, National Geophysical Data Center, Boulder, Colorado

Fahrbach, E., H. Franz, G. Gust, M. Hantel, J. Meincke, P. Müller, M. Rhein, W. Roether, and J. Willebrand (1989) Numerical Data and Functional Relationships in Science and Technology – Oceanography, Landolt–Börnstein, New Series Springer-Verlag, Berlin, Heidelberg, New York, London, Paris, Tokyo, Hong Kong, 3c, 398 pp

Frohlich, C., and R. K. Matthews (1991) Strata-Various: A Flexible Fortran Program for Dynamic Forward Modeling of Stratigraphy, Sedimentary Modeling: Computer Simulation and Methods for Improved Parameter Definition, ed. E. K. Franseen, W. L. Watney, C. G. St. C. Kendall and W. Ross , Kansas Geological Survey, 233, 449–461, 524 pp

Garde, R. J., and K. G. Ranga Raju (1977) Mechanics of Sediment Transportation and Alluvial Stream Problems, Wiley Eastern Limited, New Delhi, Bangalore, Bombay, 483 pp

Gerdes, R. (1988) Die Rolle der Dichtediffusion in numerischen Modellen der Nordatlantischen Zirkulation, Berichte aus dem Institut für Meereskunde an der Christian-Albrechts-Universität Kiel, 179, 176 pp

Gibbs, R. J., M. D. Matthews, and D. A. Link (1971) The Relationship between Sphere Size and Settling Velocity, Journal of Sedimentary Petrology, 41, No. 1, 7–18

Gibbs, R. J. (1985) Settling Velocity, Diameter, and Density for Flocs of Illite, Kaolinite, and Montmorillonite, Journal of Sedimentary Petrology, 55, 65–68

Goldschmidt, P. M., S. L. Pfirmann, I. Wollenburg, and R. Henrich (1992) Origin of Sediment Pellets from the Arctic Seafloor: Sea Ice or Icebergs?, Deep-Sea Research, 39, 539–565

Goldstein, H. (1985) Klassiche Mechanik, AULA-Verlag, Wiesbaden, 8. edition, 443 pp

Gross, T. F., and W. D. Dade (1991) Suspended Sediment Storm Modeling, Marine Geology, 99, 343–360

Haupt, B. J. (1990) Fluß-Gradient-Beziehung in wirbelauflösenden Modellen, Diplomarbeit, Institut für Meereskunde Kiel, Universität Kiel, 97 pp

Haupt, B. J., Chr. Schäfer–Neth, and K. Stattegger (1992) Towards Modelling the Paleocirculation and Sedimentation of the Northern North Atlantic, Fourth International Conference on Paleoceanography, Kiel, 137–138

Haupt, B. J., Chr. Schäfer-Neth, and K. Stattegger (1994) Modelling Sediment Drifts; A Coupled Oceanic Circulation-Sedimentation Model of the Northern North Atlantic, Paleoceanography, 9/6, 897–916

Haupt, B. J., Chr. Schäfer-Neth, and K. Stattegger (1995) 3-D Numerical Modelling of Late Quaternary Paleoceanography and Sedimentation in the Northern North Atlantic, Geologische Rundschau, 84, 137–150

Hjulström, F. (1935) Studies of the Morphological Activity of Rivers as Illustrated by the River Fyris, Bulletin of the Geological Institution of the University of Upsala, Upsala
Honjo, S. (1990) Particle Fluxes and Modern Sedimentation in the Polar Oceans, Polar Oceanography, Part B, ed. W. O. Smith Jr., Academic Press, Boston, Massachusetts, 687–739
Hsü, K. J. (1989) Physical Principles of Sedimentology, Springer-Verlag, Berlin, 231 pp
Krauß, W. (1973) Methoden und Ergebnisse der Theoretischen Ozeanographie/Methods and Results of Theoretical Oceanography – Dynamics of the Homogeneous and the Qasihomogeneous Ocean, Volume I, Gebrüder Borntraeger, Berlin, 302 pp
Krohn, J. (1975) Ein mathematisches Modell des großräumigen gezeitenbedingten Sedimenttransports mit Anwendung auf die Nordsee, Diplomarbeit, Institut für Meereskunde Hamburg
Kurz, M. (1977) Leitfäden für die Ausbildung im Deutschen Wetterdienst – Synoptische Meteorologie, Selbstverlag des Deutschen Wetterdienstes, Offenbach am Main, 8, 127 pp
LeBlond, P. H., and L. A. Mysak (1978) Waves in the Ocean, Elsevier Scientific Publishing Company, Amsterdam, Oxford, New York, 602 pp
Matthäus, D. J. (1972) Die Viskosität des Meerwassers, Beiträge zur Meereskunde, 29, 93–107
McCave, I. N. (1984) Erosion, Transport and Deposition of Fine-Grained Marine Sediments, Fine-Grained Sediments: Deep-Water Processes and Facies, ed. D. A. V. Stow and D. J. W. Piper, 35–69
McCave, I. N., and B. E. Tucholke (1986) Deep Current Controlled Sedimentation in the Western North Atlantic, The Geology of North America, ed. P. R. Vogt und B. E. Tucholke, Geological Society of America, Boulder, Colorado, M, 451–468
McCave, I. N., and T. F. Gross (1991) In-Situ Measurements of Particle Settling Velocity in Deep See, Marine Geology, 99, 403–411
Mesinger, F., and A. Arakawa (1976) Numerical Methods Used in Atmospheric Models, GARP Publication Series, 17/1, 64 pp
Middleton, G. V., and J. B. Southard (1984) Mechanics of Sediment Movement, Society of Economic Paleontologists and Mineralogists, USA, second edition, 400 pp
Miller, M. C., I. N. McCave, and P. D. Komar (1977) Threshold of Sediment Motion under Unidirectional Currents, Sedimentology, 24, 507–527
Millero, F. J., and A. Poisson, (1981) International One-Atmosphere Equation of State of Sea-Water, Deep Sea Research, 28A, 625–629
Möller, F. (1986) Einführung in die Meteorologie, Band 1: Meteorologische Elementarphänomene, B. I.-Hochschul-Taschenbücher, Band 276, Bibliographisches Institut Mannheim, Wien, Zürich, 222 pp
Paola, C., P. L. Heller, and C. L. Angevine (1992) The Large Scale Dynamics of Grain-Size Variation in Alluvial Basins, 1: Theory, Basin Research, 4, 73–90
Pickard, G. L., and W. J. Emery (1988) Descriptive Physical Oceanography – An Introduction, Pergamon Press, Oxford, 4. erweiterte Auflage, 249 pp
Pond, S., and G. L. Pickard (1986) Introductory Dynamical Oceanography, Second Edition, Pergamon Press, Oxford, 329 pp
Puls, W. (1981) Numerical Simulation of Bedform Mechanics, Mitteilungen des Instituts für Meereskunde der Universität Hamburg, Eigenverlag des Instituts für Meereskunde der Universität Hamburg, 147 Seiten
Seidov, D., M. Sarnthein, K. Stattegger, R. Prien, and M. Weinelt (1996) North Atlantic ocean circulation during the Last Glacial Maximum and subsequent meltwater event: A numerical model, J. Geophys. Res., 101, 16,305–16,332
Seidov, D., and B. J. Haupt (1997) Simulated ocean circulation and sediment transport in the North Atlantic during the last glacial maximum and today, Paleoceanography, 12, No. 2, 281–305
Shanks, A. L., and J. D. Trent (1980) Marine Snow: Sinking Rates and Potential Role in Vertical Flux, Deep-Sea Research, 27A, 137–143

Shaw, C. A., and W. W. Hay (1989) Mass-Balanced Paleographic Maps: Modeling Program and Results, Quantitative Dynamic Stratigraphy, ed. T. A. Cross, Prentice Hall, Englewood Cliffs, New Jersey, 277–291

Slingerland, R., J. W. Harbaugh, and K. P. Furlong (1994) Simulating Clastic Sedimentary Basins, Prentice Hall, Englewood Cliffs, New Jersey, 220 pp

Smolarkiewicz, P. K. (1983) A Simple Definite Advection Scheme with Small Implicit Diffusion, American Meteorological Society, 111, 479–486

Stephenson, R. (1989) Beyond First-Order Thermal Subsidence Models for Sedimentary Basins?, Quantitative Dynamic Stratigraphy, ed. T. A. Cross, Prentice Hall, Englewood Cliffs, New Jersey, 113–125

Struve, S. (1978) Transport und Vermischung einer passiven Beimengung in einem Medium mit einem vorgegebenen Geschwindigkeitsfeld, Berichte aus dem Institut für Meereskunde an der Christian-Albrechts-Universität Kiel, 57, 28 pp

Sündermann, J., and R. Klöcker (1983) Sediment Transport Modelling with Applications to the North Sea, North Sea Dynamics, ed. J. Sündermann and W. Lenz, Springer-Verlag, Berlin, Heidelberg, New York, 453–471

Syvitski, J. P. M., and S. Daughney (1992) Delta2: Delta Progradation and Basin Filling, Computer & Geosciences, 18/7, 839–897

Tetzlaff, D. M. (1989) Limits to the Predictive Ability of Dynamic Models that Simulate Clastic Sedimentation, Quantitative Dynamics Stratigraphy, ed. T. A. Cross, Prentice Hall, Englewood Cliffs, New Jersey, 55–66

Tetzlaff, D. M., and J. W. Harbaugh (1989) Simulating Clastic Sedimentation, Van Nostrand Reinhold, New York, 202 pp

UNESCO (1981) Tenth Report of the Joint Panel on Oceanographic Tables and Standards, UNESCO Technical Papers in Marine Science, 36, 24 pp

Wold, C. N. (1992) Paleobathymetry and Sediment Accumulation in the Northern North Atlantic and Southern Greenland-Iceland-Norwegian Sea, Dissertation, Mathematisch-Naturwissenschaftliche Fakultät der Universität Kiel, 255 pp

Zanke, U. (1976) Über die Naturähnlichkeit von Geschiebeversuchen bei einer Gewässersohle mit Transportkörpern, Mitteilungen des Franzius-Instituts für Wasserbau und Küsteningenieurswesen der Technischen Universität Hannover, 44, 289–324

Zanke, U. (1977a) Neuer Ansatz zur Berechnung des Transportbeginns von Sedimenten unter Strömungseinfluß, Mitteilungen des Franzius-Instituts für Wasserbau und Küsteningenieurswesen der Technischen Universität Hannover, 46, 156–178

Zanke, U. (1977b) Berechnung von Sinkgeschwindigkeiten von Sedimenten, Mitteilungen des Franzius-Instituts für Wasserbau und Küsteningenieurswesen der Technischen Universität Hannover, 46, 230–245

Zanke, U. (1978) Zusammenhänge zwischen Strömung und Sedimenttransport; Teil 1: Berechnung des Sedimenttransportes – allgemeiner Fall –, Mitteilungen des Franzius-Instituts für Wasserbau und Küsteningenieurswesen der Technischen Universität Hannover, 47, 214–345

Zanke, U. (1982) Grundlagen der Sedimentbewegung, Springer-Verlag, Berlin, Heidelberg, New York, 402 pp

## Appendix

| Symbols and definitions | | | |
|---|---|---|---|
| $c_x, c_y, c_z$ | = | Courant numbers | – |
| $C$ | = | sediment concentration in the fluid | g cm$^3$ |
| $C_n$ | = | sediment concentration at time step $n$ | g cm$^3$ |
| $d$ | = | grain size | cm |
| $d_{xi,j}, d_{yi,j}, d_{zk}$ | = | grid spacing | cm |
| $D^*$ | = | sedimentological grain diameter $\left(\frac{\rho' g}{\nu^2}\right)^{\frac{1}{3}} d$ | – |
| $FF$ | = | form factor | – |
| $g$ | = | gravitational acceleration | g cm$^{-2}$ s$^{-1}$ |
| $h_{sed}$ | = | change of bottom topography due to erosion, transport, and deposition | cm |
| $H$ | = | water depth | cm |
| $i, j, k$ | = | zonal, meridional, and vertical grid indices | – |
| $n$ | = | time step, $n$=1, 2, 3,... | – |
| $p, p_{surf}$ | = | pressure, surface pressure | g cm$^{-1}$ s$^{-1}$ |
| $q$ | = | total sediment transport | cm$^3$ cm$^{-1}$ s$^{-1}$ |
| $q_B, q_S$ | = | bed load and suspension load transport | cm$^3$ cm$^{-1}$ s$^{-1}$ |
| $Q$ | = | sediment source term | cm$^3$ cm$^{-1}$ s$^{-2}$ |
| $r_{x,n}, r_{y,n}, r_{z,n}$, $r_{bot,x,n}, r_{bot,y,n}$ | = | zonal, meridional, and vertical location inside of the numerical grid at time step $n$ | cm |
| $\vec{r}$ | = | location of a particle | cm |
| $t, t_n, t_0$ | = | time, time at time step $n$, starting time | s |
| $T$ | = | temperature | °C |
| $S$ | = | salinity | ‰ |
| $u, v, w$ | = | zonal, meridional, and vertical velocity components | cm s$^{-1}$ |
| $u_{bot}, v_{bot}$ | = | reduced zonal and meridional bottom velocity components | cm s$^{-1}$ |
| $\vec{v}, \vec{v}_{bot}$ | = | three-dimensional and two-dimensional velocity vector | cm s$^{-1}$ |
| $w_s, w_g$ | = | settling velocity, total vertical velocity | cm s$^{-1}$ |
| $x, y, z$ | = | zonal, meridional, and vertical component of the grid | cm |
| $\Delta t$ | = | time step | s |
| $\Delta x, \Delta y, \Delta z$ | = | zonal, meridional, and vertical grid spacing | cm |
| $\gamma$ | = | sediment porosity | – |
| $\nabla, \nabla_H$ | = | three- and two-dimensional Laplacian operator | cm$^{-1}$ |
| $\mu$ | = | dynamic viscosity of seawater | g cm$^{-1}$ s$^{-1}$ |
| $\nu$ | = | kinematic viscosity of seawater | cm$^2$ s$^{-1}$ |
| $\varphi$ | = | bottom slope | ° |

| Symbols and definitions | | | |
|---|---|---|---|
| $\rho_F, \rho_S$ | = | density of sea water and sediment | g $cm^{-3}$ |
| $\rho'$ | = | relative density $\frac{\rho_S - \rho_F}{\rho_F}$ | - |